

Universal impurity-assisted tunneling magnetoresistance under weak magnetic field

Oihana Txoperena,¹ Yang Song,² Lan Qing,³ Marco Gobbi,^{1,4} Luis E. Hueso,^{1,5} Hanan Dery,^{2,3} and Fèlix Casanova^{1,5}

¹*CIC nanoGUNE, 20018 Donostia-San Sebastian, Basque Country, Spain*

²*Department of Electrical and Computer Engineering,*

University of Rochester, Rochester, New York, 14627, USA

³*Department of Physics and Astronomy, University of Rochester, Rochester, New York, 14627, USA*

⁴*Université de Strasbourg, Institut de Science et d'Ingénierie Supramoléculaires (I.S.I.S.), 67083 Strasbourg, France*

⁵*IKERBASQUE, Basque Foundation of Science, 48011 Bilbao, Basque Country, Spain*

Injection of spins into semiconductors is essential for the integration of the spin functionality into conventional electronics. Insulating layers are often inserted between ferromagnetic metals and semiconductors for obtaining an efficient spin injection, and it is therefore crucial to distinguish between signatures of electrical spin injection and impurity-driven effects in the tunnel barrier. Here we demonstrate an impurity-assisted tunneling magnetoresistance effect in nonmagnetic-insulator-nonmagnetic and ferromagnetic-insulator-nonmagnetic tunnel barriers. In both cases, the effect reflects on/off switching of the tunneling current through impurity channels by the external magnetic field. The reported effect, which is universal for any impurity-assisted tunneling process, finally clarifies the controversy of a widely used technique that employs the same ferromagnetic electrode to inject and detect spin accumulation.

For the realization of semiconductor spintronic devices [1–7], the conductivity mismatch problem [8–11] and the difficulty of manipulating semiconductors at the nanoscale are the main issues delaying the progress of this research field. Employing the so-called three-terminal (3T) setup and making use of a single ferromagnetic/insulator contact for both injection and detection of spin-polarized currents was a big step towards this purpose [12]. Due to the simplicity of the micron-sized structures employed, this setup has gained popularity in semiconductor spintronics [12–19]. The Lorentzian-shaped magnetoresistance (MR) effect measured in 3T-semiconductor devices has been often attributed to spin injection on accounts of the resemblance to the celebrated Hanle effect in optical spin injection experiments [20]. However, it has been increasingly realized that the MR reported depends much on the tunneling process and too little on the semiconductor [12–19]. Furthermore, the typical junction working conditions employed for these measurements, with bias voltage settings much larger than the Zeeman energy, render the signal detection prone to subtle effects driven by impurities embedded in the tunnel barrier [13, 21].

In this Letter, we elucidate the physics behind such experiments by focusing on the study of the tunnel barriers. Accordingly, our devices render a compact geometry with an aluminum-oxide tunnel barrier created between metallic electrodes, $M_1/\text{AlO}_x/M_2$, as sketched in Fig. 1(a). The $M_1/\text{AlO}_x/M_2$ devices were fabricated in-situ in a UHV electron-beam evaporation chamber with integrated shadow masks. The base pressure of the chamber is below 10^{-9} mbar. The thickness of the top and bottom metallic electrodes, M_1 and M_2 , ranged between 10 nm and 15 nm. To systematically and decisively probe the role of impurities in the oxide, a series of devices were fabricated with 1) O_2 plasma exposure at 10^{-1} mbar at a power ranging from around 24 to 40 W for 120 seconds to 210 seconds to minimize the impurity density, or 2) n -step (n from 2 to 5) deposition of a 6 Å Al layer with subsequent oxidation of 20 min at 10^{-1} mbar of O_2 pressure with

no plasma. The latter method allows us to vary the density and locations of impurities [22, 23]. The area of the tunnel barrier ranges from $200 \times 275 \mu\text{m}^2$ to $375 \times 555 \mu\text{m}^2$. The junction resistance $R = V(0)/I$ is measured with the typical 4-point sensing configuration shown in Fig. 1(a), and the associated MR signal $\delta R(B) \equiv [V(B) - V(0)]/I$ is the ratio between the voltage change across the junction and the constant current between the metallic leads when an external magnetic field B is applied. The total amplitude of the $\delta R(B)$ signal will be called ΔR . By using metallic electrodes, we avoid the complications brought by the Fermi-level pinning when using a semiconductor [24], and we are able to establish a direct relation between the measured signals and the tunnel barrier. Most importantly, by detecting similar MR effects in ferromagnetic-insulator-nonmagnetic (FIN) and nonmagnetic-insulator-nonmagnetic (NIN) devices, we unambiguously demonstrate that the effect is entirely impurity-driven. This important finding calls for investigation of a novel effect and provides alternative interpretation to recent 3T spin injection experiments.

Figure 1(b) shows a compilation of the total amplitude of the MR effect multiplied by the total area of the tunnel barrier ($\Delta R \cdot A$) for n -step tunnel barriers with a variety of metallic electrodes, as well as $\text{Al}/\text{AlO}_x/\text{Py}$ plasma-oxidized tunnel junctions. For plasma-oxidized AlO_x , $M_1 = \text{Al}$ and $M_2 = \text{Py}$ are used (21 devices in total); and the combinations of M_1 and M_2 metals for n -step AlO_x are: $M_1 = \text{Al}$ with $M_2 = \text{Py}$ (3 devices), with $M_2 = \text{Al}$ (9 devices), with $M_2 = \text{Cu}$ (6 devices) and with $M_2 = \text{Au}$ (4 devices), and $M_1 = \text{Py}$ combined with $M_2 = \text{Au}$ (3 devices). Excluding the vast majority of the plasma-oxidized barriers, we find a power law scaling relation between $\Delta R \cdot A$ and $R \cdot A$, with an exponent factor of $1.19 (\pm 0.09)$ [dashed line in Fig. 1(b)]. In the following we focus on the results of two representative impurity-rich NIN ($\text{Al}/\text{AlO}_x/\text{Al}$) and FIN ($\text{Al}/\text{AlO}_x/\text{Py}$) devices whose tunnel barriers are fabricated by a three-step deposition procedure. Figure 1(c) shows $\delta R(B)$ of the NIN device modulated by out-of-plane (B_\perp) and in-plane (B_\parallel) fields. The full width at half maximum (FWHM) of both

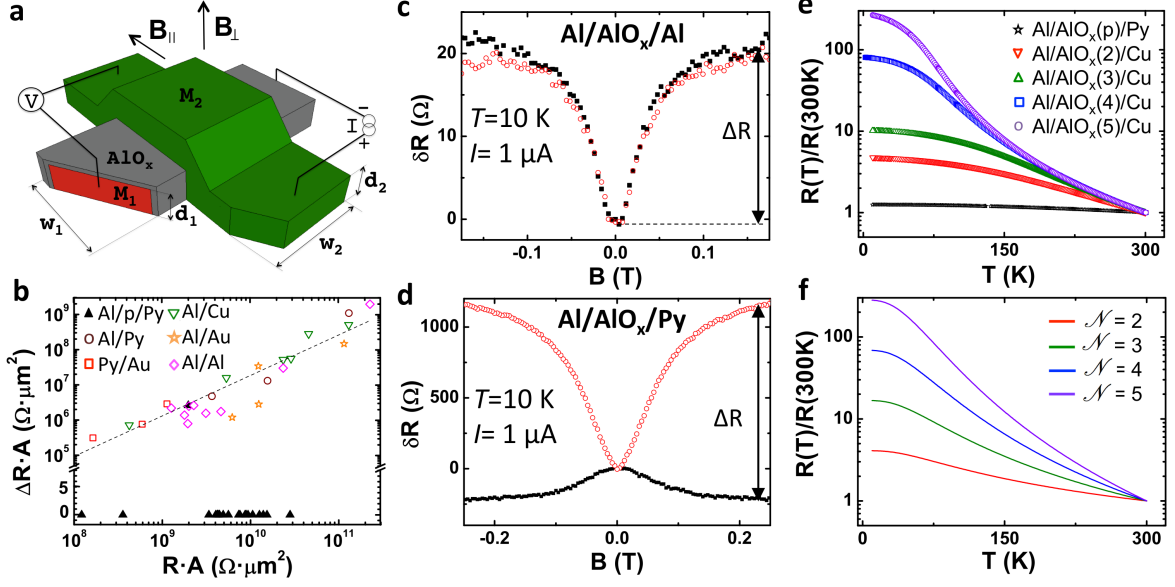


FIG. 1. Sketch of tunnel junction, its MR signals and electrical characterization. (a), A scheme of the device and its operation conditions, with the electrode dimensions tagged. (b), $\Delta R \cdot A$ as a function of the $R \cdot A$ product for different NIN and FIN devices, measured at 10 K and optimum bias conditions for each device. All the tunnel barriers are n -step (open symbols), except from the ones labeled Al/p/Py, which have plasma-oxidized tunnel barriers (solid symbols). Dashed black line is an exponential fit to the data. (c), $\delta R(B)$ of the NIN device for out-of-plane (solid symbols) and in-plane (empty symbols) field orientations measured at 10 K and 1 μ A, being $R(0) = 13.7$ k Ω under these conditions. (d), $\delta R(B)$ of the FIN device measured at 10 K and 1 μ A (injection from $M_2 = \text{Py}$ into $M_1 = \text{Al}$), with $R(0) = 158.9$ k Ω . (e), Normalized $R(T)$ for different tunnel barriers, including a plasma-oxidized barrier, Al/AIO_x(p)/Py, and n -step barriers, Al/AIO_x(n)/Cu, with $n = 2, 3, 4$ and 5. All the data have been measured at 1 μ A. (f), Theoretical $R(T)$ curves due to $\mathcal{N} - 1$ phonon-assisted hops through chains of \mathcal{N} impurities. The temperature dependence is governed by the sum of phonon emission ($n_q + 1$) and absorption (n_q), where n_q is the Bose-Einstein phonon distribution.

curves is 0.065 T and the junction resistance increases with B regardless of its orientation. We corroborated the isotropy of $\delta R(B)$ in the NIN device for more magnetic field orientations (Fig. S1 in the supplemental material). Figure 1(d) shows the respective measurements in the FIN device where the FWHM is 0.134 T (0.142 T) and the resistance increases (decreases) when applying an in-plane (out-of-plane) magnetic field. Notably, the FWHM and $\Delta R/R$ values in our devices are comparable to the recurring values seen by 3T-FIN devices employing various insulators and N materials [12–19, 25, 26].

The above results are a clear and obvious indication that the MR effect is governed by the oxide barriers rather than by non-equilibrium spin accumulation in the N leads, since no spin-polarized source is present in NIN devices. To better understand the underlying tunnel mechanism, Fig. 1(e) shows the temperature dependence of R in a series of devices with different tunnel barriers. The $R(T)$ of the plasma-oxidized junction shows a weak temperature dependence, in agreement with direct tunneling transport [27]. In contrast, the data corresponding to n -step barriers ($n = 2, 3, 4$ and 5) show a stronger T dependence. This dependence can be described by acoustic phonon-assisted tunneling through impurities that dominate the conduction and should follow $R(T) \propto [\int_0^{\epsilon_M} d\epsilon (2n_q(T) + 1) \epsilon^2]^{\mathcal{N}-1}$, where \mathcal{N} is the number of impurities assisting the tunneling event, $n_q(T) = 1/(e^{\epsilon/k_B T} - 1)$

is the Bose-Einstein distribution, and ϵ_M is the upper energy of acoustic phonons in the barrier. Figure 1(f) shows that for an n -step tunnel junction we indeed reproduce the experimental results with $\epsilon_M \sim 17$ meV [28] and $n = \mathcal{N}$, in agreement with the fabrication method employed. We obtain equivalent analysis on voltage-dependent conductance data, which is further supported by the Glazman-Matveev theory for phonon-assisted tunneling (Fig. S2 in the supplemental material) [29]. The fact that the MR effect observed in impurity-rich n -step tunnel barriers is suppressed in the plasma-oxidized ones [Fig. 1(b)] where direct tunneling is dominant confirms that the effect is entirely impurity-driven. The T and V dependence of the MR amplitude ΔR , displayed in Fig. 2, can be explained in this framework, as will be discussed below. Figures 2(a) and 2(b) show a pronounced decrease of ΔR with T for the NIN and FIN devices, respectively. Figures 2(c) and 2(d) show that, in both NIN and FIN, ΔR follows a similar voltage dependence as R , except for a sharp decrease when V is close to zero. We observe similar voltage dependences for different n -step barriers (Fig. S3 in the supplemental material).

We propose a universal tunneling mechanism to explain the experimental findings. Using the gained information regarding tunneling across impurity chains in our devices, we classify impurities with large on-site Coulomb repulsion energy ($U \gg eV$) into type A and type B classes. In type A (B), the filling energy for the first (second) electron is within the bias

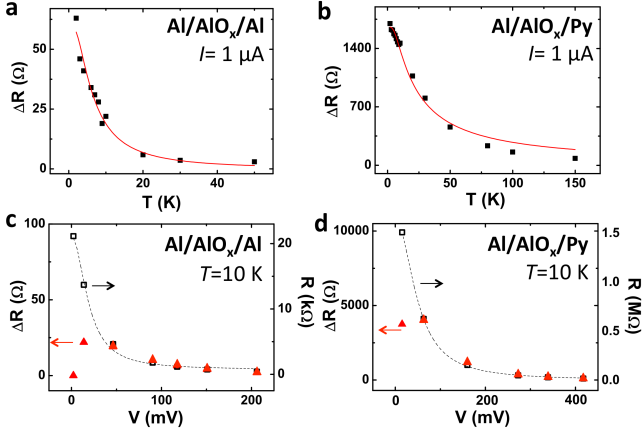


FIG. 2. Temperature and voltage dependence of the MR amplitude. (a) and (b), $\Delta R(T)$ measured at $1 \mu A$ for the NIN and FIN device, respectively. The NIN junction bias voltage changes from 14 mV at 2 K to 8 mV at 50 K, and the FIN one from 160 mV at 2 K to 120 mV at 150 K. Red solid lines are Arrhenius fits to the data with activation energies of (0.72 ± 0.07) meV for the NIN device and (1.55 ± 0.09) meV for the FIN device (see text). (c) and (d), The respective values of $\Delta R(V)$ and $R(V)$ measured at 10 K. The signals are symmetric for $V > 0$ and $V < 0$. The black dashed line is a guide to the eye.

window [30, 31]. Figure 3(a) shows an example when both types form an A-B chain in the tunnel barrier of a NIN junction. When electrons tunnel in the direction from A to B, this chain enables on (off) current switching in small (large) external magnetic fields. To understand this effect, we first focus on the steady-state spin configuration in the chain. Once an electron tunnels from the left bank into the type A impurity, it can be intuitively viewed as an ideal polarized source (‘one electron version of a half metal’). Due to Pauli blocking, this electron cannot hop to the second level of the type B impurity if the first level of the latter is filled with an electron of same spin orientation [see Fig. 3(a)]. The steady-state current across the chain is therefore blocked. This blockade can be lifted when the correlated spin configuration is randomized by spin interactions, which include the spin-orbit coupling [32], hyperfine coupling with the nuclear spin system [33], and spin-spin exchange interactions with unpaired electrons in neighboring impurities [34]. Whatever is the dominant interaction, we can invoke a mean-field approximation and view this interaction as an internal magnetic field at the impurity site that competes with the external field. When the external field is much larger than the internal fields, the type A and type B impurities in the chain see similar fields and the current is Pauli blocked as explained before. In the opposite extreme of negligible external field, on the other hand, the blockade is lifted since the correlated spin configuration is violated by spin precession about internal fields that are likely to point in different directions on the A and B sites. This behavior is illustrated by Fig. 3(b). Although A-B impurity chain is the simplest case that supports magnetic field modulation of the current, similar modulations will also occur in longer

chains in which the sequence A-B is present.

In the case of a FIN junctions, however, a single impurity chain is enough to block the current [21], which does not happen in the NIN junctions where the type A impurity within the A-B chain takes the role of F. When electrons flow from F to N (i.e. injection) through a single type B impurity, the current is completely blocked once the spin in the deep level is parallel to that of the lead. The current blockade is lifted when applying an out-of-plane field that is much smaller than the coercive field of F. Specifically, spin precession in the deep level of the type B impurity enables tunneling from the magnetic lead to the upper energy level of the impurity thereby activating this current channel. This picture explains the measured reduction in the resistance of the FIN junction for this field orientation. For the in-plane field modulation, on the other hand, the resistance increases with magnetic field, since it overcomes the precession due to internal magnetic fields, reinforcing the parallel spin configuration between spins in the deep levels of type B impurities and the spins in F. This behavior explains the measured anisotropy in $\delta R(B)$ shown in Fig. 1(d). Similarly, a single type A impurity blocks the current when electrons flow from N to F (i.e. extraction). In general, for FIN junctions, any longer impurity chain containing at least one B (A) impurity gives MR effect for injection (extraction) conditions. We note that interface roughness between F and I gives rise to stray fields [15], which in our physical picture adds to the list of internal field sources. Finally, we note that the proposed mechanism works equally well for FIN junctions where N is a semiconductor. These junctions are prone to a large density of impurities on the oxide/semiconductor atomic interface [24], and represent the main body of 3T spin injection experiments. In the supplemental material we elaborate on the manifestations of the MR effect in these junctions.

To quantify the impurity-assisted tunneling magnetoresistance effect, we describe the tunneling through two-impurity chains by generalizing the Anderson impurity Hamiltonian model to our tunneling case [29]

$$\begin{aligned}
 H = & \sum_{\ell\sigma} \left[(E_{d\ell} + \sigma E_{B\ell} \cos \theta_{\ell}) n_{d\ell\sigma} + E_{B\ell} \sin \theta_{\ell} d_{\ell\sigma}^{\dagger} d_{\ell\bar{\sigma}} \right] \\
 & + \sum_{\ell} U_{\ell} n_{d\ell\uparrow} n_{d\ell\downarrow} + \sum_{\ell\mathbf{k}\sigma} \left[\epsilon_{\mathbf{k}\ell\sigma} n_{\mathbf{k}\ell\sigma} + (V_{d\mathbf{k}\ell} \mathbf{k}_{\ell\sigma}^{\dagger} d_{\ell\sigma}^{\dagger} + \text{h.c.}) \right] \\
 & + \sum_{\mathbf{q}} \left[\epsilon_{\mathbf{q}} n_{\mathbf{q}} + V_{d\mathbf{q}} (\lambda_{\mathbf{q}} \mathbf{q}^{\dagger} + \text{h.c.}) \sum_{\sigma} (d_{L\sigma}^{\dagger} d_{R\sigma} + \text{h.c.}) \right]. \quad (1)
 \end{aligned}$$

$\sigma = -\bar{\sigma} = \pm 1$ denotes spin and $\ell = \{L, R\}$ are for Left/Right leads or impurities. d (\mathbf{k}) denotes impurity (lead) electrons and \mathbf{q} denotes phonons. The respective energy levels and occupation operators are $\{E_{d\ell}, \epsilon_{\mathbf{k}\ell\sigma}, \epsilon_{\mathbf{q}}\}$, and $\{n_{d\ell\sigma} \equiv d_{\ell\sigma}^{\dagger} d_{\ell\sigma}, n_{\mathbf{k}\ell\sigma} \equiv \mathbf{k}_{\ell\sigma}^{\dagger} \mathbf{k}_{\ell\sigma}, n_{\mathbf{q}} \equiv \mathbf{q}^{\dagger} \mathbf{q}\}$. U_{ℓ} is the on-site Coulomb repulsion energy. The Zeeman splitting energy at the ℓ -th impurity is $2E_{B\ell} \equiv g\mu_B B_{\ell}$, where \mathbf{B}_{ℓ} is the sum of internal and external magnetic fields. \mathbf{B}_L and \mathbf{B}_R define the xz plane and θ_{ℓ} is the angle between \mathbf{B}_{ℓ} and the z axis. $V_{d\mathbf{q}}$ and $V_{d\mathbf{k}\ell}$ give rise to coupling between two impurities and with their nearby leads,

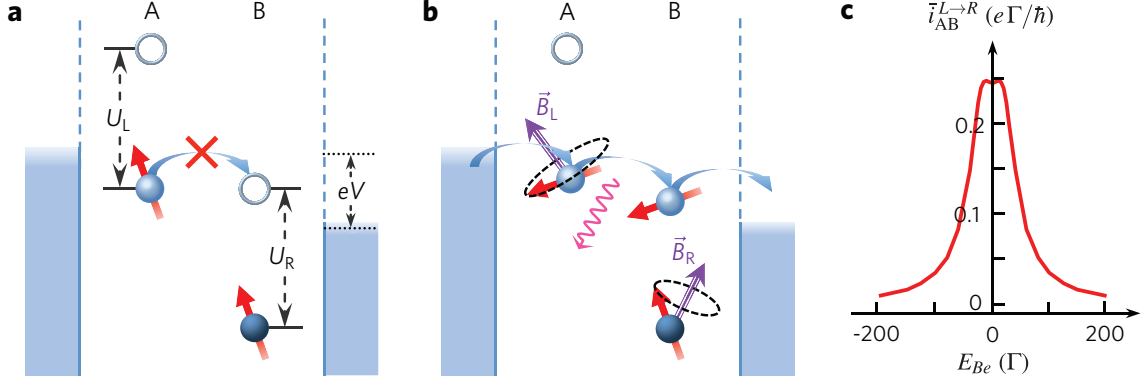


FIG. 3. Schematics for impurity-assisted MR mechanisms and the theoretical result. (a), A-B impurity chain in the bias window of a NIN junction. Due to the large on-site Coulomb repulsion ($U_\ell \gg eV$), the current across the chain is Pauli blocked when the electron spins of the lower levels in A and B are parallel. (b), The current blocking is lifted when different magnetic fields in A and B randomize the correlated spin orientation of the chain (see text). The dominant tunneling process between two impurities is assisted by phonon emission. All the rest of the possible two-impurity chains (B-A, A-A, B-B) do not modulate the current in the NIN junctions [35]. The A-B impurity chain analyzed in this figure also modulates the current in FIN devices. (c), Theoretical calculation of the current across A-B impurity chain as a function of external magnetic field for a NIN device [see text after Eq. (2)]. When the external field is much larger than the internal one, the current is blocked leading to increased resistance of the junction.

and $\lambda_{\mathbf{q}}$ is the electron-phonon interaction matrix element. We have kept only linear inelastic tunneling terms which dominate the resonant tunneling at our finite bias [29].

To find the steady-state current across the impurity chains from the above Hamiltonian, we invoke non-equilibrium Green function techniques and derive master equations in the slave-boson representation [36, 37]. The detailed master equations are given in the supplemental material. They describe the competition between the Zeeman terms, impurity-lead coupling (Γ_ℓ) and inter-impurity coupling (Γ_{dd}). The latter two in the weak coupling regime are expressed by $\Gamma_\ell = 2\pi \sum_{\mathbf{k}} |V_{\ell\mathbf{k}}|^2 \delta(E_{d\ell} - \epsilon_{\mathbf{k}\ell})$ and $\Gamma_{dd} = 4\pi \sum_{\mathbf{q}} |V_{dd}\lambda_{\mathbf{q}}|^2 \delta(\Delta E_d - \epsilon_{\mathbf{q}})$, respectively, where $\Delta E_d = E_{dL} - (E_{dR} + U_R)$. We can solve the master equations for the particular case of the A-B impurity chain and bias setting described in Fig. 3, obtaining the following steady-state solution for the dominant contribution where $\Delta E_d \gg k_B T$ (i.e. $n_q \ll 1$)

$$i_{AB}^{L \rightarrow R}(\theta) \approx \frac{2q}{\hbar} \left(\frac{1}{\Gamma_L} + \frac{1}{\Gamma_R} - \frac{1}{\Gamma_L + \Gamma_R} + \frac{4}{\Gamma_{dd} \sin^2 \theta} \right)^{-1}. \quad (2)$$

This expression describes the magnetic-field modulated current via an A-B impurity chain, where the magnetic field dependence is manifested via the angle $\theta = \theta_R - \theta_L$. For large enough external field (\mathbf{B}_e) the effective fields in the left and right impurities are aligned ($\mathbf{B}_L \parallel \mathbf{B}_R$), and the current is blocked (i.e., $\theta \rightarrow 0$ leading to $i_{AB}^{L \rightarrow R} \rightarrow 0$). When B_e is much smaller than the internal fields, on the other hand, $\langle \sin^2 \theta \rangle$ is effectively of the order of 1/2 after averaging over the distribution of θ , and the current can flow. The full expression for $i_{AB}^{L \rightarrow R}$ is given in Eq. (S2) of the supplemental material, and in Eq. (2) above we show its simplified form in the limit that $\{E_{B_L}, E_{B_R}, |E_{B_L} - E_{B_R}|\} \gg \{\Gamma_R, \Gamma_L, \Gamma_{dd}\}$. This limit is gener-

ally satisfied due to the random distribution of internal fields whose magnitudes and variations can readily exceed those of the weak coupling parameters (Γ 's). In this limit, the FWHM are determined by the characteristic amplitude of the internal fields. This explains why the stray fields that add to the internal fields in the FIN give rise to somewhat larger FWHM values compared to NIN [see Figs. 1(c) and 1(d)], as well as the independence of the measured FWHM values on the thickness of the tunnel barrier. Equation (2) shows a series-like resistance for the A-B chain where the negative term, $-1/(\Gamma_L + \Gamma_R)$, stems from the coherence between two impurities [35].

We can now recover the measured signal by noting that

$$\frac{\delta R(\mathbf{B}_e)}{R} = N_{AB} \times \frac{\bar{i}_{AB}^{L \rightarrow R}}{I}, \quad (3)$$

where N_{AB} is the number of A-B chains with $U_\ell \gg eV$, and I is the total current enabled via tunneling over impurity clusters with various sizes and on-site repulsion U 's.

All the obtained experimental results are readily understood by applying the above analysis. First, Fig. 3(c) shows an example of a current simulation using Eq. (2) after averaging over the amplitude and orientation of the internal fields. We have used $\Gamma_L = \Gamma_R = \Gamma_{dd} = \Gamma$, and modeled the internal field in each of the impurities as an independent normalized Gaussian distribution whose mean and standard deviation are 20Γ and 6Γ , respectively [35]. We can observe that the shape of the simulated curve is in agreement with the Lorentzian shape measured in both NIN and FIN [Figs. 1(c) and 1(d)]. Second, we explain the $\Delta R(T)$ behavior for the NIN and FIN devices. On the one hand, we observe a stronger T dependence of the signal for NIN than for FIN [see Figs. 2(a) and 2(b)]. The origin for this behavior is that in NIN devices the blockade is effective when $U_\ell \gg eV$ for both impurities on

the A-B chain. By contrast, in the FIN devices, it is sufficient to have one such impurity due to the spin polarization of F, rendering ΔR less temperature dependent. Using this information, $\Delta R(T)$ can be fitted by a typical Arrhenius law $\delta R(T) \propto [1 - \exp(-E_a/k_B T)]^m$ where $m = 2(1)$ for NIN (FIN) devices. The red lines in Figs. 2(a) and 2(b) show the dependence where the activation energy is $E_a = 0.72 \pm 0.07$ meV for the NIN device and $E_a = 1.55 \pm 0.09$ meV for the FIN device. The activation energy around $E_a \sim 1$ meV is associated with the threshold of small impurities to merge into larger clusters resulting in $U \lesssim eV$ [34]. This scenario is compatible with our devices, where, apart from isolated impurities, we might also have impurities in close proximity behaving as big clusters as temperature is increased. Third, the decrease of $\Delta R(V)$ at low bias values [Figs. 2(c) and 2(d)] is because of the vanishing number of A-B channels within the small bias window. Finally, related to that, the relative signal $\Delta R/R$ is a result of the small portion of A-B chains with $U_\ell \gg eV$ among all cluster chains. The fact that $\Delta R/R$ is nearly constant comparing all devices, as shown in Fig. 1(b), is in agreement with Eq. (3).

In conclusion, the MR effect shows how the impurity-assisted tunnel resistance can be modulated by a magnetic field when the Zeeman splitting of the impurity spin states is smaller compared to the applied bias voltage. Other impurity-driven effects reported up to date, such as the Kondo effect or Coulomb correlation in resonant tunneling [38, 39], appear in the opposite regime at strong magnetic fields. This mechanism therefore promises new possibilities to explore local states in disordered materials or nanostructures. Our analysis puts NIN and FIN junctions on an equal footing, with the physical picture readily generalizable to chains with $\mathcal{N} \geq 2(1)$ impurities in NIN (FIN) junctions. This novel magnetoresistance effect is general for any impurity-assisted tunneling process regardless of the oxide thickness or materials used. Therefore, the presented work will be used as a benchmark to spin injection experiments to any nonmagnetic material, and specially will redirect research of semiconductor spintronics, with all the implications in such a technologically relevant area.

The authors acknowledge Dr. A. Bedoya-Pinto for fruitful discussions. The work in Spain is supported by the European Union 7th Framework Programme (NMP3-SL-2011-263104-HINTS, PIRG06-GA-2009-256470 and the European Research Council Grant 257654-SPINTROS), by the Spanish Ministry of Economy under Project No. MAT2012-37638 and by the Basque Government under Project No. PI2011-1. The work in USA is supported by NRI-NSF, NSF, and DTRA Contracts No. DMR-1124601, ECCS-1231570, and HDTRA1-13-1-0013, respectively.

-
- [1] Y. K. Kato, R. C. Myers, A. C. Gossard, and D. D. Awschalom, *Science* **306**, 1910 (2004).
 - [2] S. Murakami, N. Nagaosa, and S.-C. Zhang, *Science* **301**, 1348 (2003).
 - [3] I. Zutic, J. Fabian, and S. D. Sarma, *Rev. Mod. Phys.* **76**, 323 (2004).
 - [4] H. Dery, P. Dalal, Ł. Cywiński, and L. J. Sham, *Nature* **447**, 573 (2007).
 - [5] S. A. Crooker *et al.*, *Science* **309**, 2191 (2005).
 - [6] I. Appelbaum, B. Huang, and J. Monsma, *Nature* **447**, 295 (2007).
 - [7] P. Li, J. Li, L. Qing, H. Dery, and I. Appelbaum, *Phys. Rev. Lett.* **111**, 257204 (2013).
 - [8] M. Johnson and R. H. Silsbee, *Phys. Rev. B* **35**, 4959 (1987).
 - [9] G. Schmidt, D. Ferrand, L. W. Molenkamp, A. T. Filip, and B. J. van Wees, *Phys. Rev. B* **62**, R4790 (2000).
 - [10] E. I. Rashba, *Phys. Rev. B* **62**, R16267 (2000).
 - [11] A. Fert and H. Jaffres, *Phys. Rev. B* **64**, 184420 (2001).
 - [12] S. P. Dash, S. Sharma, R. S. Patel, M. P. de Jong, and R. Jansen, *Nature* **462**, 491 (2009).
 - [13] M. Tran *et al.*, *Phys. Rev. Lett.* **102**, 036601 (2009).
 - [14] C. H. Li, O. M. G. van 't Erve, and B. T. Jonker, *Nature Commun.* **2**, 245 (2011).
 - [15] S. P. Dash *et al.*, *Phys. Rev. B* **84**, 054410 (2011).
 - [16] Y. Aoki *et al.*, *Phys. Rev. B* **86**, 081201(R) (2012).
 - [17] A. Jain *et al.*, *Phys. Rev. Lett.* **109**, 106603 (2012).
 - [18] T. Uemura, K. Kondo, J. Fujisawa, K.-I. Matsuda, and M. Yamamoto, *Appl. Phys. Lett.* **101**, 132411 (2012).
 - [19] S. Sharma, *et al.*, *Phys. Rev. B* **89**, 075301 (2014).
 - [20] F. Meier and B. P. Zakharchenya, Ed., *Optical Orientation* (North-Holland, New York, 1984).
 - [21] Y. Song and H. Dery, arXiv:1401.7649 (2014).
 - [22] O. Txoperena *et al.*, *Appl. Phys. Lett.* **102**, 192406 (2013).
 - [23] W. H. Rippard, A. C. Perrella, F. J. Albert, and R. A. Buhrman, *Phys. Rev. Lett.* **88**, 046805 (2002).
 - [24] S. M. Sze, *Physics of Semiconductor Devices* (Wiley, New York, 1981).
 - [25] O. M. J. van 't Erve *et al.*, *Nature Nanotechnol.* **7**, 737 (2012).
 - [26] W. Han *et al.*, *Nature Commun.* **4**, 2134 (2013).
 - [27] J. J. Åkerman *et al.*, *J. Magn. Magn. Mater.* **240**, 86-91 (2002).
 - [28] R. Heid, D. Strauch, and K.-P. Bohnen, *Phys. Rev. B* **61**, 8625 (2000).
 - [29] L. I. Glazman and K. A. Matveev, *Zh. Eksp. Teor. Fiz.* **94**, 332 (1988) [*Sov. Phys. JETP* **67**, 1276 (1988)].
 - [30] L. I. Glazman and K. A. Matveev, *Pis'ma Zh. Eksp. Teor. Fiz.* **48**, 403 (1988) [*JETP Lett.* **48**, 445 (1988)].
 - [31] H. Bahlouli, K. A. Matveev, D. Ephron, and M. R. Beasley, *Phys. Rev. B* **49**, 14496 (1994).
 - [32] R. Prioli and J. S. Helman, *Phys. Rev. B* **52**, 7887 (1995).
 - [33] M. Boero, A. Pasquarello, J. Sarnthein, and R. Car, *Phys. Rev. Lett.* **78**, 887 (1997).
 - [34] J. S. Helman and B. Abeles, *Phys. Rev. Lett.* **37**, 1429 (1976).
 - [35] See Supplemental Material online.
 - [36] Z. Zou and P. W. Anderson, *Phys. Rev. B* **37**, 627(R) (1988).
 - [37] J. C. Le Guillou and E. Ragoucy, *Phys. Rev. B* **52**, 2403 (1995).
 - [38] D. Goldhaber-Gordon, *et al.*, *Nature* **391**, 156 (1998).
 - [39] D. Ephron, Y. Xu, and M. R. Beasley, *Phys. Rev. Lett.* **69**, 3112 (1992).
-

Supplemental Material for “Universal impurity-assisted tunneling magnetoresistance under weak magnetic field”

Oihana Txoperena, Yang Song, Lan Qing, Marco Gobbi,
Luis E. Hueso, Hanan Dery, Fèlix Casanova

Additional Experimental Results and Discussion

In Fig. S1, we show two additional magnetic field (B) directions applied on the representative NIN device. We observe no correlation between the MR signals and the \mathbf{B} field directions.

Figure S2 characterizes the tunnel junctions for the representative 3-step NIN and FIN devices at small bias windows. The left panels show their voltage dependence at $eV \gg k_B T$ while the right panels show their temperature dependence at $k_B T \gg eV$. In these regimes we can apply Glazman-Matveev theory for ordinary hopping via impurity chains [S1,S2]. We fit the obtained data by $G(V) = c_1 + c_2 V^p$ and $G(T) = c_3 + c_4 T^p$, where $p = \mathcal{N} - 2/(\mathcal{N} + 1)$ with \mathcal{N} being the average impurity number in the chains under these small bias windows. From the voltage-dependent measurements, we obtain $\mathcal{N} = 2.088 \pm 0.008$ for the NIN sample and $\mathcal{N} = 2.12 \pm 0.04$ for the FIN sample. From the temperature-dependent ones, we obtain $\mathcal{N} = 2.39 \pm 0.06$ for the NIN sample and $\mathcal{N} = 2.2 \pm 0.2$ for the FIN sample. Therefore, the results

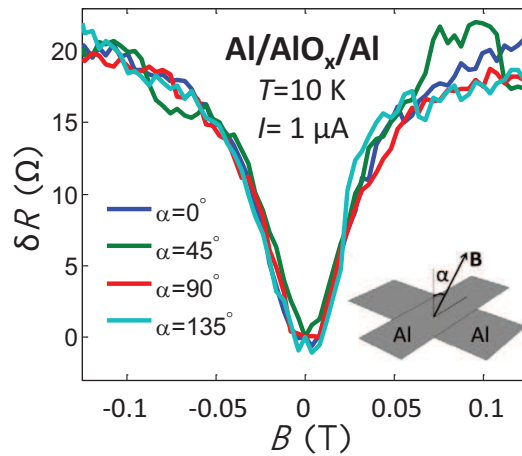


FIG. S1. The isotropy of MR signal in NIN device with respect to magnetic field directions. Four different magnetic field directions (see inset) are applied on the Al/AlO_x(3-step)/Al device, which we focus on in the main text. The measurements are done at 10 K and 1 μ A.

obtained from the voltage- and temperature-dependent measurements are consistent, and show that at these small bias windows the transport in our 3-step tunnel barriers is dominated by conduction through two-impurity chains, meaning $\mathcal{N} \approx n - 1$, where n is the number of steps of the tunnel barrier. Note that in such small bias window condition, we can observe a perceivable background of V and T independent conductance due to direct and resonant tunneling, which becomes negligible in the usual working condition (e.g. $1 \mu\text{A}$ constant current in Fig. 1(c) and 1(d) of the main text). The average impurity number \mathcal{N} slowly increases as the bias window increases [S2], as under the condition used in Fig. 1(e) of the main text where the number of impurity is closer to the number of deposition steps, $\mathcal{N} \approx n$. Finally, we point out that the above theoretical results [S1] are applicable only when $\max\{eV, k_B T\} \lesssim \epsilon_M$, where ϵ_M is the maximum acoustic phonon energy. We obtain that ϵ_M is on the order of 17 meV from Fig. 1(e) and 1(f) of the main text. It is worth noting that in Fig. 1(e) we have $eV > \{k_B T, \epsilon_M\}$, and in this case the only important temperature dependence comes from that of the phonon population.

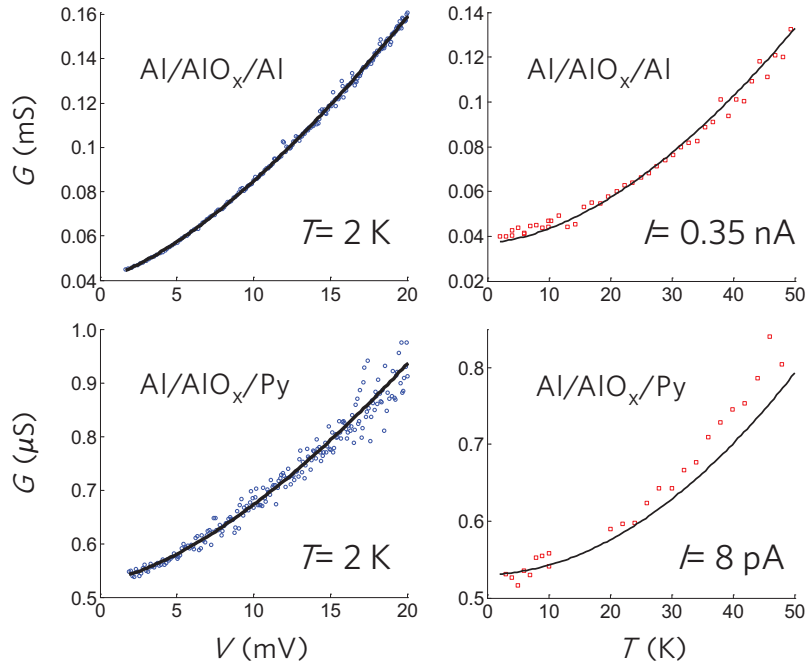


FIG. S2. Total conductance $G = 1/R$ for the representative 3-step NIN and FIN devices as a function of voltage and temperature under small bias windows. The voltage dependence is measured at $eV \gg k_B T$, and the temperature dependence is measured at $k_B T \gg eV$ where V is on the order of $10 \mu\text{V}$ in both devices. Circles are measured data and solid lines are the theoretical fitting for phonon-assisted tunneling via impurities (see text).

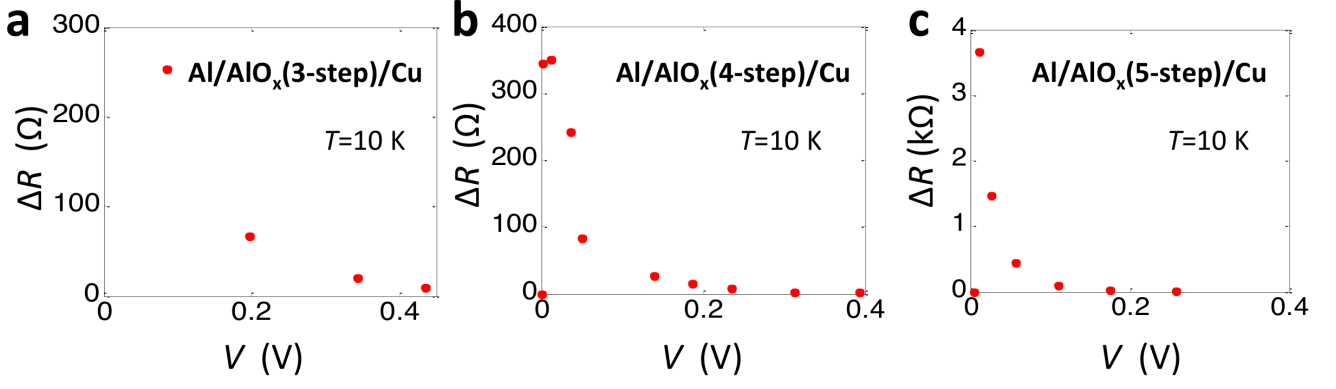


FIG. S3. Bias dependence of the MR signal ΔR for Al/AlO_x/Cu devices, with (a) 3-step, (b) 4-step and (c) 5-step tunnel barriers. All the measurements are done at 10 K.

Figure S3 shows $\Delta R(V)$ of several Al/AlO_x(n)/Cu samples, with comparable voltage dependences to those shown in Fig. 2 of the main text. At large voltage values, ΔR follows the same voltage dependence as the total tunnel resistance, as explained by Eq. 3 of the main text. However, when the bias window reduces significantly, the small portion of impurity chains that are subject to magnetic field modulation (i.e., chains with an A-B sequence) becomes basically non-available compared to the total impurity chains, as well as to the direct and resonant tunneling channels. As a result, there are sharp drops of ΔR as the voltage is close to zero. It is worth pointing out that the voltage value where ΔR is maximum, V_{max} , decreases as n increases, with $V_{max}=85$ mV, 12 mV and 5 mV for $n=3$, 4 and 5, respectively. This can be qualitatively explained as follows: the higher the n is, the longer the impurity chains are, and the more probable is to find A-B chains fulfilling $U_\ell \gg eV$, obtaining MR at smaller bias values.

Numerical calculations

Master equations and the full analytical expression

The general master equations for the A-B tunneling chain, under arbitrary magnetic fields on the two impurity sites and phonon population $n_{\mathbf{q}}$, are given below. The basis states can be understood as $|n_L n_R\rangle$, where $n = \{0, \uparrow, \downarrow, 2\}$ has four possible states. We define density operators by $\hat{\rho}_{m_L m_R}^{n_L n_R} \equiv |n_L n_R\rangle \langle m_L m_R|$ and

$\hat{\rho}_{n_L n_R} \equiv \hat{\rho}_{n_L n_R}^{n_L n_R}$. Without loss of generality, we set $\theta_L = 0$, $\theta_R = \theta_R - \theta_L = \theta$, and choose $E_{dL} > E_{dR}$.

$$\hbar \frac{d}{dt} \rho_{0\sigma} = -2\Gamma_L \rho_{0\sigma} + \Gamma_R \rho_{02} - 2E_{B_R} \sin \theta \text{Im} \rho_{0\sigma}^{0\bar{\sigma}}, \quad (\text{S1a})$$

$$\begin{aligned} \frac{d}{dt} \rho_{02} = & -2(\Gamma_L + \Gamma_R) \rho_{02} \\ & + \Gamma_d [-2n_{\mathbf{q}} \rho_{02} + (n_{\mathbf{q}} + 1)(\rho_{\uparrow\downarrow} + \rho_{\downarrow\uparrow} - 2\text{Re} \rho_{\uparrow\downarrow}^{\downarrow\uparrow})], \end{aligned} \quad (\text{S1b})$$

$$\begin{aligned} \hbar \frac{d}{dt} \rho_{\sigma\bar{\sigma}} = & \Gamma_L \rho_{0\bar{\sigma}} + \Gamma_R \rho_{\sigma 2} + 2E_{B_R} \sin \theta \text{Im} \rho_{\sigma\bar{\sigma}}^{\sigma\bar{\sigma}} \\ & + \Gamma_d [n_{\mathbf{q}} \rho_{02} + (n_{\mathbf{q}} + 1)(-\rho_{\sigma\bar{\sigma}} + \text{Re} \rho_{\sigma\bar{\sigma}}^{\sigma\bar{\sigma}})], \end{aligned} \quad (\text{S1c})$$

$$\hbar \frac{d}{dt} \rho_{\sigma 2} = \Gamma_L \rho_{02} - 2\Gamma_R \rho_{\sigma 2}, \quad (\text{S1d})$$

$$\hbar \frac{d}{dt} \rho_{\sigma\sigma} = \Gamma_L \rho_{0\sigma} + \Gamma_R \rho_{\sigma 2} - E_{B_R} \sin \theta \text{Im} \rho_{\sigma\sigma}^{\sigma\bar{\sigma}}, \quad (\text{S1e})$$

$$\begin{aligned} \hbar \frac{d}{dt} \rho_{\uparrow\downarrow}^{\downarrow\uparrow} = & \Gamma_d [-n_{\mathbf{q}} \rho_{02} + (n_{\mathbf{q}} + 1)(\rho_{\uparrow\downarrow} + \rho_{\downarrow\uparrow} - 2\rho_{\uparrow\downarrow}^{\downarrow\uparrow})/2] \\ & + 2i(-E_{B_L} + E_{B_R} \cos \theta) \rho_{\uparrow\downarrow}^{\downarrow\uparrow} + iE_{B_R} \sin \theta (\rho_{\uparrow\downarrow}^{\downarrow\downarrow} - \rho_{\uparrow\downarrow}^{\uparrow\uparrow}), \end{aligned} \quad (\text{S1f})$$

$$\hbar \frac{d}{dt} \rho_{0\uparrow}^{0\downarrow} = -2\Gamma_L \rho_{0\uparrow}^{0\downarrow} + iE_{B_R} [-2\cos \theta \rho_{0\uparrow}^{0\downarrow} + \sin \theta (\rho_{0\uparrow} - \rho_{0\downarrow})], \quad (\text{S1g})$$

$$\hbar \frac{d}{dt} \rho_{\uparrow 2}^{\downarrow 2} = -2\Gamma_R \rho_{\uparrow 2}^{\downarrow 2} - 2iE_{B_L} \rho_{\uparrow 2}^{\downarrow 2}, \quad (\text{S1h})$$

$$\hbar \frac{d}{dt} \rho_{\uparrow\uparrow}^{\downarrow\downarrow} = -2i(E_{B_L} + E_{B_R} \cos \theta) \rho_{\uparrow\uparrow}^{\downarrow\downarrow} + iE_{B_R} \sin \theta (\rho_{\uparrow\uparrow}^{\downarrow\uparrow} - \rho_{\uparrow\downarrow}^{\downarrow\downarrow}), \quad (\text{S1i})$$

$$\begin{aligned} \hbar \frac{d}{dt} \rho_{\sigma\bar{\sigma}}^{\sigma\bar{\sigma}} = & \Gamma_L \rho_{0\bar{\sigma}}^{0\bar{\sigma}} + \Gamma_d (n_{\mathbf{q}} + 1)(\rho_{\sigma\bar{\sigma}}^{\sigma\bar{\sigma}} - \rho_{\sigma\bar{\sigma}}^{\sigma\bar{\sigma}})/2 \\ & + iE_{B_R} [-2\sigma \cos \theta \rho_{\sigma\bar{\sigma}}^{\sigma\bar{\sigma}} + \sin \theta (\rho_{\sigma\sigma} - \rho_{\sigma\bar{\sigma}})], \end{aligned} \quad (\text{S1j})$$

$$\begin{aligned} \hbar \frac{d}{dt} \rho_{\sigma\bar{\sigma}}^{\bar{\sigma}\sigma} = & \Gamma_L \rho_{\sigma 2}^{\bar{\sigma} 2} + \Gamma_d (n_{\mathbf{q}} + 1)(\rho_{\sigma\bar{\sigma}}^{\bar{\sigma}\sigma} - \rho_{\sigma\bar{\sigma}}^{\bar{\sigma}\sigma})/2 \\ & - 2\sigma iE_{B_L} \rho_{\sigma\bar{\sigma}}^{\bar{\sigma}\sigma} + iE_{B_R} \sin \theta (\rho_{\sigma\bar{\sigma}}^{\bar{\sigma}\sigma} - \rho_{\sigma\bar{\sigma}}^{\bar{\sigma}\sigma}), \end{aligned} \quad (\text{S1k})$$

The equations are not all independent but supplemented by $1 = \rho_{02} + \sum_{\sigma} (\rho_{0\sigma} + \rho_{\sigma\bar{\sigma}} + \rho_{\sigma 2} + \rho_{\sigma\sigma})$. Having solutions to all matrix elements at $n_{\mathbf{q}} \ll 1$, and $I = \frac{q}{\hbar} 2\Gamma_L (\rho_{0\uparrow} + \rho_{0\downarrow} + \rho_{02})$, we get

$$I = \frac{8q}{\hbar} (\Gamma_L + \Gamma_R) \Gamma_d \Gamma_L \Gamma_R E_{B_L}^2 E_{B_R}^2 (E_{B_L}^2 - E_{B_R}^2)^2 \sin^2 \theta / \Lambda, \quad (\text{S2})$$

where

$$\begin{aligned}\Lambda = & (E_{B_L}^2 + E_{B_R}^2 + 2E_{B_L}E_{B_R}\cos\theta)\Gamma_d^2\Gamma_L\Gamma_R(\Gamma_L + \Gamma_R) \times \\ & [E_{B_L}^4 - E_{B_L}^2E_{B_R}^2(1 + \cos^2\theta) + E_{B_R}^4] + 4E_{B_L}^2E_{B_R}^2(E_{B_L}^2 - E_{B_R}^2)^2 \\ & \times [\Gamma_d(\Gamma_L^2 + \Gamma_L\Gamma_R + \Gamma_R^2)\sin^2\theta + 4\Gamma_L\Gamma_R(\Gamma_L + \Gamma_R)],\end{aligned}$$

Equation S2 leads to the approximated form in Eq. 2. The negative term in Eq. 2 is a consequence of physical invariance under the rotation of spin coordinate, and it also occurs in B-A, A-A and B-B chains whose currents are independent of magnetic field. It is reflected in the off-diagonal elements in the master Eqs. S1.

Calculation of averaged current expressions via AB chains, as well as on BA, AA, and BB chains

In the following we show how to obtain the averaged current expression plotted in Fig. 3(c) starting from the full current expression via an AB chain shown in Eq. S1. To do that, we need to integrate over the internal field distributions at the two impurities, taking into account that they experience local internal magnetic fields due to spin interactions in addition to the external field. In order to do the integration, we express E_{B_L} , E_{B_R} and $\sin\theta$ in Eq. S1 in terms of the left and right internal fields \mathbf{B}_{i_L} and \mathbf{B}_{i_R} , and external field \mathbf{B}_e . If z direction is set along \mathbf{B}_e , from $\mathbf{B}_{L(R)} = \mathbf{B}_{i_{L(R)}} + \mathbf{B}_e$ one can obtain

$$B_\ell = \sqrt{B_{i_\ell}^2 + B_e^2 + 2B_{i_\ell}B_e\cos\theta_{i_\ell}}, \quad \cos\theta_\ell = \frac{B_{i_\ell}\cos\theta_{i_\ell} + B_e}{B_\ell}, \quad \text{and} \quad \phi_\ell = \phi_{i_\ell}, \quad (\text{S3})$$

where $\ell = L, R$. The angle θ between \mathbf{B}_L and \mathbf{B}_R can be expressed as follows

$$\cos\theta = \cos\theta_L\cos\theta_R + \sin\theta_L\sin\theta_R\cos(\phi_L - \phi_R). \quad (\text{S4})$$

As previously mentioned, the averaged current is a result of integration over internal field distribution

probability $\mathcal{F}_\ell(B_{i_\ell}, \theta_\ell, \phi_\ell)$,

$$\bar{i}_{AB} = \int d^3\mathbf{B}_{i_L} \int d^3\mathbf{B}_{i_R} (\mathcal{F}_L \times \mathcal{F}_R \times i_{AB}), \quad (\text{S5})$$

where $\int d^3\mathbf{B}_\ell \mathcal{F}_\ell = 1$ and, for simplicity, we assume that \mathcal{F}_L and \mathcal{F}_R are independent. For example, we may assume they are Gaussian distributions with finite variation around a mean value on the radial direction. Figure 3(c) is obtained in this way by a straightforward numerical integration of Eq. S5. We assume $\Gamma_L = \Gamma_R = \Gamma_{dd}$ because at this condition the impurity-assisted inelastic tunneling current is maximum [S1,S2].

For the purpose of gaining more insight of the magnitude of the signal and its trend with external magnetic field, we can make justified simplifications in order to carry out analytical integration. Since we are interested mainly in the regime of average internal field and its variation much larger than the tunneling rate, $\{E_{B_L}, E_{B_R}, |E_{B_L} - E_{B_R}|\} \gg \{\Gamma_R, \Gamma_L, \Gamma_{dd}\}$, we can properly use the approximation in Eq. 2 of the main text. Doing so, for any $\mathcal{F}_{L,R}$ with spherical symmetry, at $B_e = 0$ we have

$$\begin{aligned} \bar{i}_{AB}(B_e = 0) &\approx \frac{e}{\hbar} \frac{8\pi^2 \Gamma_d \Lambda_1}{\Lambda_2} \left[1 - \frac{\Lambda_1 \operatorname{arctanh}\left(\sqrt{\frac{\Lambda_2}{\Lambda_2 + \Lambda_1}}\right)}{\sqrt{\Lambda_2(\Lambda_2 + \Lambda_1)}} \right] \int_0^\infty dB_{i_L} B_{i_L}^2 \mathcal{F}_L(B_{i_L}) \int_0^\infty dB_{i_R} B_{i_R}^2 \mathcal{F}_R(B_{i_R}) \\ &= \frac{e}{\hbar} \frac{\Gamma_d \Lambda_1}{2\Lambda_2} \left[1 - \frac{\Lambda_1 \operatorname{arctanh}\left(\sqrt{\frac{\Lambda_2}{\Lambda_2 + \Lambda_1}}\right)}{\sqrt{\Lambda_2(\Lambda_2 + \Lambda_1)}} \right] \end{aligned} \quad (\text{S6})$$

where

$$\Lambda_1 = 2\Gamma_L \Gamma_R (\Gamma_L + \Gamma_R), \quad \Lambda_2 = \frac{1}{2} \Gamma_d (\Gamma_L^2 + \Gamma_L \Gamma_R + \Gamma_R^2). \quad (\text{S7})$$

We have $\bar{i}_{AB}(B_e = 0) \approx 0.257 \Gamma_e / \hbar$ well matching the numerical result in Fig. 3(c), with the corresponding parameters used $\Gamma_L = \Gamma_R = \Gamma_{dd} = \Gamma$ and $\mathcal{F}_\ell \propto \exp[-(E_{Bi_\ell} - 20\Gamma)^2 / 2(6\Gamma)^2]$.

In order to obtain an approximate but analytical trend of the current as a function of external field B_e , we

can further approximate by using $i_{AB} \approx \Gamma_d \sin^2 \theta e / 2\hbar$, obtaining

$$\begin{aligned}
\bar{i}_{AB}(B_e) &\approx \frac{e}{2\hbar} \Gamma_d \int d^3 \mathbf{B}_{iL} \int d^3 \mathbf{B}_{iR} \mathcal{F}_L(B_{iL}) \mathcal{F}_R(B_{iR}) \\
&\quad \left\{ 1 - \left[\frac{B_{iL} \cos \theta_{iL} + B_e}{B_L} \frac{B_{iR} \cos \theta_{iR} + B_e}{B_R} + \frac{B_{iL} \sin \theta_{iL}}{B_L} \frac{B_{iR} \sin \theta_{iR}}{B_R} \cos(\phi_{iL} - \phi_{iR}) \right]^2 \right\} \\
&= \frac{e}{2\hbar} \Gamma_d - \pi^2 \frac{e}{\hbar} \Gamma_d \left[\int_0^\infty dB_{iL} \int_0^\infty dB_{iR} \mathcal{F}_L(B_{iL}) \mathcal{F}_R(B_{iR}) (B_{iL} B_{iR})^2 \right. \\
&\quad \left. \int_{-1}^1 dz_L \int_{-1}^1 dz_R \frac{2(B_{iL} z_L + B_e)^2 (B_{iR} z_R + B_e)^2 + B_{iL}^2 (1 - z_L^2) B_{iR}^2 (1 - z_R^2)}{(B_{iL}^2 + B_e^2 + 2B_{iL} B_e z_L)(B_{iR}^2 + B_e^2 + 2B_{iR} B_e z_R)} \right] \\
&= \frac{e}{2\hbar} \Gamma_d \left\{ 1 - \frac{\pi^2}{8} \left(76 - \frac{100}{3} \right) \left(\int_0^\infty dB_i \mathcal{F}(B_i) B_i^2 \right)^2 \right. \\
&\quad \left. - \frac{\pi^2}{8} \frac{1}{B_e^6} \left(\int_0^\infty dB_i \mathcal{F}(B_i) B_i \left[\frac{2}{\sqrt{3}} B_e B_i (5B_e^2 - 3B_i^2) - \sqrt{3} (B_e^2 - B_i^2)^2 \ln \frac{|B_e - B_i|}{B_e + B_i} \right] \right)^2 \right\} \\
&\approx \frac{e}{\hbar} \Gamma_d \left\{ \frac{1}{3} - \frac{1}{768 B_e^6 \bar{B}_i^2} \left(2B_e \bar{B}_i (3\bar{B}_i^2 - 5B_e^2) + 3(\bar{B}_i^2 - B_e^2)^2 \ln \frac{|B_e - \bar{B}_i|}{B_e + \bar{B}_i} \right)^2 \right\}. \tag{S8}
\end{aligned}$$

where in the last step we have used the condition that the mean magnetic field \bar{B}_i of the distribution $\mathcal{F}_{i\ell}$ is much larger than its standard deviation, and replaced $\ln[|B_e - B_i|/(B_e + B_i)]$ by $\ln[|B_e - \bar{B}_i|/(B_e + \bar{B}_i)]$ in the integrand (this excellent approximation has been checked numerically for the whole range of B_e/\bar{B}_i).

Last, we show explicitly that the current via other two-impurity chain types BA, AA and BB is magnetic field independent for the NIN devices. They are obtained by exactly solving similar master equations as those shown Eq. S1.

$$i_{BA} = \frac{e}{\hbar} \frac{2\Gamma_d \Gamma_L \Gamma_R (\Gamma_L + \Gamma_R) (n_{\mathbf{q}} + 1)}{\Gamma_L \Gamma_R (\Gamma_L + \Gamma_R + 2\Gamma_d n_{\mathbf{q}}) + 2\Gamma_d (\Gamma_L^2 + \Gamma_L \Gamma_R + \Gamma_R^2) (n_{\mathbf{q}} + 1)}, \tag{S9}$$

$$i_{AA} = \frac{e}{\hbar} \frac{2\Gamma_d \Gamma_L \Gamma_R (2\Gamma_L + \Gamma_R) (n_{\mathbf{q}} + 1)}{2\Gamma_L \Gamma_R (2\Gamma_L + \Gamma_R + 2\Gamma_d n_{\mathbf{q}}) + \Gamma_d (4\Gamma_L^2 + 2\Gamma_L \Gamma_R + \Gamma_R^2) (n_{\mathbf{q}} + 1)}, \tag{S10}$$

$$i_{BB} = \frac{e}{\hbar} \frac{2\Gamma_d \Gamma_L \Gamma_R (\Gamma_L + 2\Gamma_R) (n_{\mathbf{q}} + 1)}{2\Gamma_L \Gamma_R (\Gamma_L + 2\Gamma_R + 2\Gamma_d n_{\mathbf{q}}) + \Gamma_d (\Gamma_L^2 + 2\Gamma_L \Gamma_R + 4\Gamma_R^2) (n_{\mathbf{q}} + 1)}. \tag{S11}$$

Discussion of New Experimental Results from Other Groups

The mechanism proposed in the main text can readily explain the recurring magnetic field modulated signals from most 3T-FIN experiments when N is a semiconductor. The commonly seen feature that the

MR signals depend less on the lead materials but more on the barriers is consistent with our framework. Here we manifest the versatility of this theory by explaining in detail some new observations that cannot be explained by previous theories [S3].

First, the Fe/MgO/Si devices in Ref. [S3] show coexistence of two effects: the total tunnel resistance R saturates when the oxide barrier becomes ultrathin, whereas the MR signal ΔR shows a robust exponential dependence on the thickness of the oxide barrier. This phenomena can be straightforwardly explained by our tunneling theory of a FIN junction via one impurity, which is most likely to reside at impurity-prone atomic interface between the oxide (MgO) and the Schottky barrier in the Si region. The total tunnel resistance saturation is a typical behavior of resonant tunneling via a single impurity. When the thickness t of the MgO barrier is significantly reduced ($\ln \Gamma_{\text{Fe}} \propto -t$), the resonant resistance is dominated by the smaller tunneling rate Γ_{Si} ($\ll \Gamma_{\text{Fe}}$) yielding

$$I_{\text{res}} = \frac{2e}{\hbar} \frac{\Gamma_{\text{Fe}} \Gamma_{\text{Si}}}{\Gamma_{\text{Fe}} + \Gamma_{\text{Si}}} \approx \frac{2e}{\hbar} \Gamma_{\text{Si}}. \quad (\text{S12})$$

Therefore, the tunneling resistance becomes constant, since Γ_{Si} is determined by the Schottky barrier which remains the same regardless of the MgO thickness.

Concerning the magnitude of the MR current Δi , we can see that when $\Gamma_{\text{Si}} \ll \Gamma_{\text{Fe}}$ it depends on the relative difference of the spin-dependent resonant tunneling rates, $p^2 \Gamma_{\text{Si}} / (1 - p^2) \Gamma_{\text{Fe}}$, in addition to Γ_{Si} . $\Gamma_{\text{Fe}} = (\Gamma_{\text{Fe}\uparrow} + \Gamma_{\text{Fe}\downarrow})/2$ and p are the spin-average tunneling rate and the spin polarization of the ferromagnet, and the p^2 dependence stems from the additional current-induced spin polarization of the impurity. Since ferromagnets are not pure half metal and p is a fraction of 1, the intuitive current on/off picture induced by the magnetic field becomes effectively the difference of resonant tunneling rates from two opposite spins. When the tunnel barrier is really thin, their difference becomes extremely small because even the minority spin resonant tunneling rate between Fe and the impurity is much larger than that between Si and the impurity. As a result, the bottleneck of the ‘current-blocked state’ is caused by the Schottky barrier in

the Si region rather than the minority spin tunneling from Fe. So the magnetic field modulation tends to be suppressed in this limit. More quantitative analysis is found in Ref. [S4].

All in all, we have

$$\Delta i \propto \Gamma_{\text{Si}}^2 / \Gamma_{\text{Fe}}. \quad (\text{S13})$$

Combining Δi and I_{res} with Eq. 3 of the main text, we have $\Delta R \propto 1/\Gamma_{\text{Fe}}$ for $\Gamma_{\text{Si}} \ll \Gamma_{\text{Fe}}$. In the other limit of thick MgO barrier ($\Gamma_{\text{Si}} \gg \Gamma_{\text{Fe}}$), both I_{res} and Δi are proportional to Γ_{Fe} . The magnetic modulation in this case is effective where Δi is governed by the large relative difference p^2 . Again, we have $\Delta R \propto 1/\Gamma_F$. The two proportionality prefactors are of the same order of magnitude. Our MR picture leads to the overall exponential dependence of ΔR on the oxide thickness. This dependence has also been seen by other groups [S5]. The remaining control experimental results of Ref. [S3] are naturally understood within this MR picture. Replacing Si with metal eliminates the impurity-prone MgO/Si interface and Schottky barrier, therefore suppressing the impurity-assisted TMR. Inserting non-magnetic layer into the Fe/MgO interface turns off the spin polarization source [S3], and again suppresses our one-impurity-assisted TMR effect in FIN devices.

A noteworthy difference between FIN junctions where N is a semiconductor or a metal is the absence of the Schottky barrier in the latter ones. In both cases, treating the tunnel barrier by plasma oxidation is likely to eliminate the impurities inside the oxide layer. But defects can still be produced on the atomic interface between two different materials. When N is a semiconductor, the resonance current via impurities on the atomic interface between the oxide and the Schottky barrier can be large, and the MR signal comes from those impurities with large on-site Coulomb repulsion. When N is a metal, on the other hand, the tunnel current via impurities at the oxide/metal interface is negligible because the density of states in N is much higher than that of the impurities. This difference can then explain the negligible MR signal in our plasma-oxidized samples where both leads are metallic, and its appearance in experiments when N is a

semiconductor.

[S1] L. I. Glazman, K. A. Matveev, Zh. Eksp. Teor. Fiz. **94**, 332 (1988), [Sov. Phys. JETP **67**, 1276 (1988).]

[S2] Y. Xu, D. Ephron, M. R. Beasley, Phys. Rev. B **52**, 2843 (1995).

[S3] S. Sharma *et al.*, Phys. Rev. B **89**, 075301 (2014).

[S4] Y. Song, H. Dery, arXiv: 1401.7649 (2014).

[S5] T. Uemura, K. Kondo, J. Fujisawa, K.-I. Matsuda, M. Yamamoto, Appl. Phys. Lett. **101**, 132411 (2012).
